Molecular Dynamics Simulation of Heat Conduction in Near-Critical Fluids

Toshiyuki Hamanaka, Ryoichi Yamamoto, and Akira Onuki
Department of Physics, Kyoto University, Kyoto 606-8502, Japan
(Dated: March 22, 2022)

Using molecular dynamics simulations we study supercritical fluids near the gas-liquid critical point under heat flow in two dimensions. We calculate the steady-state temperature and density profiles. The resultant thermal conductivity exhibits critical singularity in agreement with the mode-coupling theory in two dimensions. We also calculate distributions of the momentum and heat fluxes at fixed density. They indicate that liquid-like (entropy-poor) clusters move toward the warmer boundary and gas-like (entropy-rich) regions move toward the cooler boundary in a temperature gradient. This counterflow results in critical enhancement of the thermal conductivity.

PACS numbers: 64.60.Ht, 64.70.Fx, 61.20.Ja

I. INTRODUCTION

In one-component fluids, the density and energy fluctuations are known to become long-ranged and long-lived as the temperature T and the density n approach the critical values $T_{\rm c}$ and $n_{\rm c}$ [1, 2]. The critical singularities are characterized by the correlation length ξ, which grows as $\xi_0(T/T_{\rm c}-1)^{-\nu}$ on the critical isochore with ξ_0 being a microscopic length and ν being the critical exponent. On one hand, the isothermal compressibility K_T, the isobaric thermal expansion coefficient α_p, and the isobaric specific heat C_p grow as $\xi^{2-\hat{\eta}}$, with $\hat{\eta}$ being the small Fisher critical exponent. On the other hand, the thermal diffusivity D_T behaves as $k_{\rm B}T/\eta\xi^{d-2}$ and the life time of the critical fluctuations grows as $\tau_\xi = \xi^2/D_T \sim \xi^d$, where d is the space dimensionality and the weak singularity of the shear viscosity η is neglected. As a result, the thermal conductivity $\lambda = D_T C_p$ grows as $\xi^{4-d-\hat{\eta}}$. The critical behavior of λ and η has been well described by the mode-coupling theory [3, 4] and by the dynamic renormalization group theory [5].

However, the calculations in these dynamical theories are performed in the space of the wave vector of the fluctuations and are rather formal. The real space picture of the enhanced heat transport in a small temperature gradient dT/dz is as follows [2]. The critical fluctuations with relatively higher (lower) densities should be convected in the direction (reverse direction) of the temperature gradient. The typical velocity of the clusters with lengths of order ξ is given by

$$v_\xi \sim (\xi/\xi_0)^{\beta/\nu+2-\hat{\eta}} \frac{D_T}{T}\frac{dT}{dz}, \tag{1}$$

in the linear response with β being the critical exponent. The entropy of the liquid-like regions is smaller than that of the gas-like regions by $n\xi^d\delta s \sim \xi^{d-\beta/\nu}$, where the entropy fluctuation δs (as well as the denisity fluctuation δn) has sizes typically of order $\xi^{-\beta/\nu}$ ($\sim (T/T_{\rm c}-1)^\beta$ on the critical isochore). The thermal average of the convective heat flux $nT\delta s v_\xi$ thus gives rise to the critical heat conduction. Within their life times the clusters can move only over the distance,

$$v_\xi\tau_\xi \sim \frac{\Delta n}{n}(\xi/\xi_0)^{\beta/\nu}\xi^2/L, \tag{2}$$

where $\Delta n = \alpha_p L dT/dz$ is the difference between the densities at the two ends of the cell. This distance is very short for L much longer than ξ. Hence it should be difficult to unambiguously observe the the cluster motion in heat flow experimentally and even numerically.

As numerical work of heat conduction in fluids [6, 7], the thermal conductivity has been calculated using equilibrium MD simulations [8, 9] on the basis of the Green-Kubo formula [2, 6] or using nonequilibrium MD simulations [10, 11, 12]. In particular, developing a simple method, Ohara performed nonequilibrium MD simulations for Lenard-Jones (LJ) fluids [13] and for liquid water [14]. All these previous papers treated fluids far from the critical point. In this paper we will use Ohara's method to realize heat-conducting states in the one-phase region near the critical point.

This paper is organized as follows. In Section 2 we will present numerical results on equilibrium critical behavior in supercritical LJ fluids. In Section 3 we will show numerical results on near-critical heat conduction together with theoretical interpretations. In particular, we will confirm the cluster convection mechanism by introducing steady-state distributions of the momentum and heat fluxes at fixed density. In Appendix B we will summarize the mode-coupling theory for the thermal conductivity. In Appendix C we will examine the linear response to heat flow and justify Eq.1.

II. MODEL AND EQUILIBRIUM RESULTS

We used a two-dimensional (2D) LJ fluid composed of N identical particles. The pair potential as a function of the distance r between two particles is given by

$$\phi(r) = 4\epsilon\left[\left(\frac{\sigma}{r}\right)^{12} - \left(\frac{\sigma}{r}\right)^{6}\right] - C \quad (r \le r_{\rm c}), \tag{3}$$

and $\phi(r) = 0$ for $r > r_{\rm c}$. The constant C is chosen such that $\phi(r_{\rm c}) = 0$. The cut-off length $r_{\rm c}$ was set equal to 3σ.

TABLE I: Numerical estimations for the two-dimensional LJ fluids. The estimated critical temperature T_c and density n_c are given in the first and second columns. The particle number N and the cut-off radius r_{cut} used are given in the third and fourth columns.

T_c	n_c	N	r_{cut}	Source
0.533	0.335	256		[15]
0.472	0.33	500	∞^a	[16]
0.515	0.355	512	∞^a	[17]
0.459	0.35	512	2.5	[17]
0.498	0.36	8000	∞^a	[18]
0.47	0.35	4096	2.5	[19]
0.47	0.37	5000	3.0	Present work

[a]The Gibbs ensemble method was used with $r_{cut} = L/2$, where L is the cell size.

The system contains $N = 5000$ particles. Space and time are measured in units of σ and $\tau_0 = (m\sigma^2/\epsilon)^{1/2}$, where m is the particle mass. Equilibrium states of the fluid may be characterized by the temperature T and the average number density $n = N/V$ measured in units of ϵ/k_B and σ^{-2}, respectively. The pressure is measured in units of $\sigma^{-2}\epsilon$. We used the leapfrog algorithm to integrate the Newton differential equations with a time step of 0.01 and the cell-index method of cutting off the interaction potential. The details of these numerical methods are described in the literature [7].

The phase diagram of the two-dimensional LJ fluid has been studied by several groups using the conventional Monte Carlo method [15], the Gibbs ensemble method [16, 17, 18], and finite-size scaling analysis [19]. Table I summarizes the critical parameters reported in the literature together with our MD results. However, note that the critical parameters largely depend on the details of the truncation of the potential [17]. We also mention that Luo *et al* [20] examined thermal relaxation in a two-dimensional supercritical LJ fluid.

As preliminary work before nonequilibrium simulations, we carried out equilibrium simulations in the canonical (constant-NVT) ensemble, using the Nose-Hoover thermostat [7, 21] under the periodic boundary condition, with $\Delta t = 0.01$, to calculate the structure factor $S(q)$. We started with random initial particle configurations at each given temperature, waited for $t_w = 5 \times 10^4$, and afterward took data in a subsequent time interval of $t_w < t < 2t_w$. This long equilibration is needed because the density fluctuations relax very slowly near the critical point. That is, t_w should be longer than the life time $\tau_\xi = \xi^2/D_T$ of the critical fluctuations with sizes of the order of the correlation length ξ [2]. Here λ is the thermal conductivity and C_p is the isobaric heat capacity per unit volume, respectively. In particular, in two dimensions the critical exponent ν is equal to 1 and the critical singularity of D_T is weak (as will be evident in Eq.19), so on the critical isochore τ_ξ grows as

$$\tau_\xi \sim \xi^2 \sim (T/T_c - 1)^{-2} \quad (d = 2). \tag{4}$$

We consider the structure factor given by

$$S(q) = \int d\boldsymbol{r} e^{i\boldsymbol{q}\cdot\boldsymbol{r}} \langle \hat{n}(\boldsymbol{r}, t)\hat{n}(\boldsymbol{0}, t)\rangle/n. \tag{5}$$

Here we define the fluctuating particle number density in terms the particle positions as

$$\hat{n}(\boldsymbol{r}, t) = \sum_{i=1}^{N} \delta(\boldsymbol{r}_i(t) - \boldsymbol{r}). \tag{6}$$

We took the angle average in the calculation of $S(q)$. Fig.1 shows $S(q)$ for $T = 0.65$, 0.51, 0.5, 0.495, and 0.49 at $n = 0.37$. We can see the power law q behavior,

$$S(q) \sim q^{-7/4}, \tag{7}$$

in the range $\xi^{-1} \lesssim q \lesssim 2$ near the critical point, where the exponent value 7/4 is consistent with the well-known Fisher critical exponent $\hat{\eta} = 1/4$ in two dimensions. The peak around $q \sim 6$ represents the short-range pair correlation at this density. We then determined the correlation length ξ by fitting the data to the extrapolated expression $S(q) = nk_BTK_T/[1 + (q\xi)^2]^{7/8}$ for $q \ll 1$. The isothermal compressibility $K_T = (\partial n/\partial p)_T/n$ can be determined from the long wavelength limit of $S(q)$. We show ξ vs n in Fig.2 and K_T vs n in Fig. 3 for various $T(\geq 0.49)$. Although not shown in Figs.2 and 3, we also performed simulations at lower temperatures to obtain $\xi \sim 50$ for $T = 0.485$ and $\xi > L$ (apparently) for $T = 0.48$ at $n = 0.37$. However, for these T, our simulation times are not sufficiently long compared with τ_ξ in Eq.4. From the peak positions in Figs.2 and 3 we estimated $n_c \cong 0.37$ in Table 1. This value was also obtained as the mean position of the two peaks in the one-body density distribution $\Psi(\rho)$ (defined by Eq.22 below) in equilibrium for $0.495 \leq T \leq 0.50$.

From the data in Figs.2 and 3 on the critical isochore, K_T behaves as a function of ξ as

$$K_T = 3.7\xi^{7/4} + 0.80, \tag{8}$$

in units of σ^2/ϵ. We then fitted ξ to the scaling form $\xi = \xi_0(T/T_c - 1)^{-1}$ on the critical isochore to obtain $T_c = 0.47$ and $\xi_0 = 0.6$. From the isothermal curves in the $p - n$ plane in the range $0.495 \leq T \leq 0.50$ at $n = n_c$, we obtained[22]

$$\left(\frac{\partial p}{\partial T}\right)_n \cong \left(\frac{\partial p}{\partial T}\right)_{cx} \cong 0.40. \tag{9}$$

We also consider the specific heat $C_p = nT(\partial s/\partial T)_p$ per unit volume (s being the entropy per particle) and the thermal expansion coefficient $\alpha_p = -(\partial n/\partial T)_p/n$ at constant pressure. These quantities grow strongly and are related to K_T by [2]

$$C_p \cong T\left(\frac{\partial p}{\partial T}\right)_{cx}^2 K_T, \quad \alpha_p \cong \left(\frac{\partial p}{\partial T}\right)_{cx} K_T, \tag{10}$$

near the critical point. These relations will be used in the next section.

As long as $\xi \ll L$, our equilibrium results are consistent with the well-known results of critical phenomena [1, 2]. If ξ approaches L, the finite-size scaling analysis may be performed [19]. However, such analysis is beyond the scope of this paper.

III. NONEQUILIBRIUM SIMULATIONS

A. Method

Next we imposed a heat flux to the system using Ohara's method [13, 14]. As illustrated in Fig.4, the cell is divided into three parts, cooling, heating, and interior regions. In the cooling region $-0.5L < z < -0.4L$ the average temperature of the particles was kept at $T_{\rm L}$, while in the heating region $0.4L < z < 0.5L$ it was kept at $T_{\rm H}$. The precise definition of the average temperature in a given region will be presented in Eq.12 below. The pinning of the average temperatures in the cooling and heating regions was realized by simple scaling of the velocities of the particles in the two regions at every time step. The periodic boundary condition was imposed in the x direction, while the walls at $z = \pm L/2$ were assumed to interact with the particles via the LJ potential in Eq.3 where r is the distance from the wall and $r_{\rm c} = 3$. The particles in the interior ($-0.4L < z < 0.4L$) obeyed the Newtonian dynamics without artificial thermostat. The particles entering the interior from the cooling (heating) region have lower (higher) kinetic energies than those of the particles in the interior on the average. Then a steady heat conducting state is realized after a transient time.

In our nonequilibrium simulations, we used a single density $n = 0.37$ nearly equal to $n_{\rm c}$. The system length is then $L = (5000/0.37)^{1/2} = 116$. The lower boundary temperature $T_{\rm L}$ was changed as 0.7, 0.65, 0.6, 0.52, 0.505, 0.5, 0.495, and 0.49. The temperature difference $\Delta T = T_{\rm H} - T_{\rm L}$ was fixed at 0.005 in all the simulations. We regard the system to be in a steady state for $t > t_{\rm w} = 6 \times 10^4$ after application of ΔT. In the following the steady-state values of the physical quantities will be the time averages over the data during the next time interval $t_{\rm w} < t < t_{\rm w} + t_{\rm data}$ with $t_{\rm data} = 14 \times 10^4$.

B. Steady-state density and temperature profiles

Fig.5 displays a snapshot of the particle positions in the cell at $t = 2 \times 10^5$ for $T_{\rm L} = 0.50$, where the system is nearly in a steady state. The large clusters formed by many particles are significantly denser near the cooler boundary (bottom) than near the warmer boundary (top)[23]. This is due to the diverging isobaric thermal expansion as will be shown in Eq.16 below. By comparing successive snapshots (not shown here), we recognize that the clusters appear and disappear continuously on the time scale of τ_ξ in Eq.4.

To quantitatively analyze Fig.5, we need to calculate the time averages of the temperature and the density. They are defined as follows. Dividing the interior into eight layers with thickness $L/10$, the density in the ℓ-th layer is defined by $n_\ell(t) = (10/L^2)N_\ell(t)$ in terms of the particle number in the ℓ-th layer,

$$N_\ell(t) = \int_{z_\ell}^{z_{\ell+1}} dz \int_0^L dx \hat{n}(\boldsymbol{r}, t), \tag{11}$$

where $z_\ell = (\ell - 5)L/10$ and $\hat{n}(\boldsymbol{r}, t)$ is the fluctuating density in Eq.6. The temperature in the ℓ-th layer $T_\ell(t)$ may be defined by

$$T_\ell(t) = \frac{1}{N_\ell(t)} \sum_{i \in \ell} |\boldsymbol{v}_i(t) - \bar{\boldsymbol{v}}_\ell(t)|^2, \tag{12}$$

where the summation is over the particles within the ℓ-th layer and $\bar{\boldsymbol{v}}_\ell(t) = \sum_{i \in \ell} \boldsymbol{v}_i(t)/N_\ell(t)$ is the average velocity within the ℓ-th layer. Notice that the 0-th layer is the cooling region and the 9-th layer is the heating region. Thus we set $T_0(t) = T_{\rm L}$ and $T_9(t) = T_{\rm H}$ in the cooling and heating regions, respectively.

Fig.6 shows the steady-state temperature and density profiles,

$$T(z) = \langle T_\ell(t) \rangle, \quad n(z) = \langle n_\ell(t) \rangle, \tag{13}$$

which are the time averages with $z = (\ell - 5)L/10$. Here $T_{\rm L} = 0.50$ and $n = 0.37$ as in Fig.5. For this case the deviation of $T(z)$ from the linear profile is not large and there exists a temperature gradient also in the cooling and heating regions. We may define the penetration widths $d_{\rm L}$ and $d_{\rm H}$ by the extrapolations,

$$T(-d_{\rm L} - 2L/5) = T_{\rm L}, \quad T(2L/5 + d_{\rm H}) = T_{\rm H}. \tag{14}$$

When the temperature profile is nearly linear, we simply find $d_{\rm L} \cong d_{\rm H} \cong L/20$. When the temperature flux is not too large, the effective cell length of heat conduction becomes

$$4L/5 + d_{\rm L} + d_{\rm H} \cong 9L/10, \tag{15}$$

which is the distance between the middle points of the cooling and heating region as in the case of Ohara's simulation [13].

On the other hand, in Fig.6 the density deviation is much more enhanced than that of the temperature. We expect that if the deviation $\delta T(z) = T(z) - T(0)$ (measured from the center $y = 0$) is not too large, the average density deviation $\delta n(z) = n(z) - n(0)$ should be given by

$$\delta n(z) \cong -n \alpha_p \delta T(z), \tag{16}$$

where α_p is the isobaric thermal expansion coefficient. Here, at the center, we find $T(0) = 0.5025$ and $n(0) = 0.37$, so Eq.10 indicates $K_T = 159$ and $n\alpha_p = 23.5$

at the center. In Fig.6 the solid line has a slope of $\Delta T/(9L/10) = 0.0056/L$, while the dotted line a slope of $-23.5 \times 0.0056/L$. These two lines can fairly fit the temperature and density data, though there are considerable deviations close to the boundaries (obviously because the boundary regions are considerably off-critical). Notice that we assume homogeneity of the pressure in Eq.16. To check this, we calculated the steady-state time averages of the trace of the stress tensor (integrated in each layer) and found no appreciable heterogeneity in these values.

C. Thermal conductivity

In our simulations, the steady-state thermal conductivity λ in the interior was calculated from

$$\lambda = Q\frac{0.9L}{\Delta T}, \tag{17}$$

where $0.9L$ is the effective cell length in Eq.15. The Q is the steady-state heat flux written as

$$Q = -\langle J_0^{Qz}(t)\rangle/0.8L^2 \tag{18}$$

where $J_0^{Qz}(t)$ is the integral of the heat flux density within the interior with area $0.8L^2$ and its microscopic expression will be given in Appendix A. In our small system the fluctuations of the heat flux turned out to be large, so we performed 10 independent runs and calculated the mean values of the corresponding 10 time averages. In Fig.7 the thermal conductivity data are shown as a function of the temperature at the critical density, which gives the background $\lambda_{\rm B} = 2.3$ far above the critical point. In Fig.8 the data of the singular part $\Delta\lambda = \lambda - \lambda_{\rm B}$ are plotted as a functions of ξ. For $\xi \lesssim 10$ our numerical data nicely agree with the theoretical linear response result Eq.19, which will be explained below. For $\xi \gtrsim 10$ the finite-size effect and the nonlinear response effect should be responsible for the saturation of the calculated λ.

The mode-coupling theory in Appendix B predicts the following behavior,

$$\begin{aligned}\lambda &= \lambda_{\rm B} + \frac{T}{4\pi\eta}C_p \ln(L/\xi) \\ &= \lambda_{\rm B} + A_\lambda \xi^{7/4}\ln(L/\xi),\end{aligned} \tag{19}$$

where η is the shear viscosity [25]. See also Appendix C for the linear response theory for heat flow. The singular part of the thermal conductivity is simply given by $D_T C_p$ with D_T being the thermal diffusion constant [4]. In terms of the isothermal compressibility K_T the coefficient A_λ is written as

$$A_\lambda = \frac{T^2}{4\pi\eta}\left(\frac{\partial p}{\partial T}\right)^2_{\rm cx} K_T \xi^{-7/4}. \tag{20}$$

To estimate A_λ from the above expression, we calculated the shear viscosity η at $T = 0.50$ and $n = 0.37$ by two methods and obtained almost the same results. That is, (i) the time integral of the stress time-correlation function [6, 7] in the range $0 < t < 100$ gave $\eta \cong 0.35$ and (ii) the long time tail of the velocity correlation function gave $\eta \cong 0.33$ (see Appendix D). If we use the latter result together with Eqs.7 and 8, we are led to $A_\lambda = 0.035$. In Fig.8 the theoretical curve represents the second term on the right hand side of Eq.19 with this A_λ. It excellently agrees with the data before the saturation of λ.

D. Momentum and heat flux distributions at fixed density under heat flow

Some characteristic features of the density fluctuations can be seen in the one-body density distribution function $\Psi(\rho) = \langle\delta(\hat{n}_{\rm cell} - \rho)\rangle$, where $\hat{n}_{\rm cell}$ is the density in an appropriately chosen cell in the fluid and the average is taken over the thermal fluctuations and over the cells in the system [17, 18, 19, 24]. It is the probability distribution of the coarse-grained density. Furthermore, in the presence of heat flow, we are interested in distributions of the momentum and heat fluxes at fixed density. They can give the correlations between these fluxes and the density within the same cell even if the cluster motion driven by heat flow is very small.

First we coarse-grain the system to calculate $\Psi(\rho)$. The interior region ($-0.4L < z < 0.4L$ and $0 < y < L$) is divided into 10×10 rectangular subsystems. Let $M_k(t)$ ($k = 1, \cdots, 100$) be the particle number in the k-th cell at time t. After the time averaging in steady states, we obtained the distribution of $M_k(t)$ for integer M as

$$P(M) = \frac{1}{100}\sum_{k=1}^{100}\langle\delta_{M,M_k(t)}\rangle, \tag{21}$$

where $\delta_{M,M'}$ is the Kronecker delta, and $\sum_{M=0}^{\infty} P(M) = 1$ by definition. For each given density $\rho = M/V_{\rm cell}$ we define

$$\begin{aligned}\Psi(\rho) &= V_{\rm cell}P(V_{\rm cell}\rho) \\ &= \frac{1}{100}\sum_{k=1}^{100}\langle\delta(\rho - n_k(t))\rangle,\end{aligned} \tag{22}$$

where $V_{\rm cell} = 0.8L^2/100$ is the cell volume and the second line is the expression in the continuum limit with $n_k(t) = M_k(t)/V_{\rm cell}$. By definition we obtain

$$\int_0^\infty d\rho\Psi(\rho) = 1, \quad \int_0^\infty d\rho\rho\Psi(\rho) = n_{\rm in}, \tag{23}$$

where $n_{\rm in}$ is the average density in the interior and $n_{\rm in} \cong n$ in our case. The second moment becomes

$$\int_0^\infty d\rho(\rho - n_{\rm in})^2\Psi(\rho) = \frac{1}{100}\sum_{k=1}^{100}\langle(n_k(t) - n_{\rm in})^2\rangle. \tag{24}$$

In equilibrium, or if the heterogeneity along the heat flow is neglected, the second moment behaves as $\xi^{2-\hat{\eta}}/V_{\rm cell}$ for

ξ less than the cell length but as $V_{\rm cell}^{(2-d-\hat{\eta})/d}$ for larger ξ due to the finite-size effect.

Now we consider the coarse-grained momentum and heat fluxes at fixed density. We calculate the following steady-state averages,

$$J_p(\rho) = \frac{1}{100V_{\rm cell}} \sum_{k=1}^{100} \langle J_{0k}^z(t)\delta(\rho - n_k(t))\rangle \qquad (25)$$

$$J_Q(\rho) = \frac{1}{100V_{\rm cell}} \sum_{k=1}^{100} \langle J_{0k}^{Qz}(t)\delta(\rho - n_k(t))\rangle, \qquad (26)$$

where $J_{0k}^z(t)$ and $J_{0k}^{Qz}(t)$ are the z component of the space integral of the momentum density and that of the heat flux, respectively, within the k-th cell (see (A.2) in the Appendix A for their definitions). If they are divided by the cell volume $V_{\rm cell}$, they become the coresgrained densities, respectively. For simplicity, we may write $\Psi(\rho) = \langle \delta(\rho - \hat{n})\rangle$, $J_p(\rho) = \langle J_z \delta(\rho - \hat{n})\rangle$ and $J_Q(\rho) = \langle J_z^Q \delta(\rho - \hat{n})\rangle$ regarding the dynamic variables involved as the coarse-grained quantities. The normalized quantities $J_p(\rho)/\Psi(\rho)$ and $J_Q(\rho)/\Psi(\rho)$ may be interpreted as the coarse-grained conditional average of the momentum density and that of the heat flux, respectively, under the condition of fixed density at ρ. If integrated over ρ, we obtain

$$\int_0^\infty d\rho J_p(\rho) = 0, \qquad (27)$$

$$\int_0^\infty d\rho J_Q(\rho) = -Q, \qquad (28)$$

where Q is the average heat flux defined by Eq.18 in the interior. In Appendix C we will examine the expected behavior of these quantities using the linear response theory for ∇T [26].

In Fig.9 we show the three quantities, $\Psi(\rho)$, $J_p(\rho)$, and $J_Q(\rho)$, obtained from 10 independent runs. The temperature at $z = L$ is $T_{\rm L} = 0.65$ in (a) (upper plate), $T_{\rm L} = 0.5$ in (b) (middle plate), and $T_{\rm L} = 0.48$ in (c)(lower plate), with $\Delta T = 0.005$ or $\langle dT/dz\rangle = 0.43 \times 10^{-4}$. As can be seen in Fig.7, the calculated thermal conductivity is $\lambda = 5.96$ in (a), 5.66 in (b), and 2.63 in (c). Salient features are as follows.
(i) The density distribution $\Psi(\rho)$ has a rather sharp peak in (a), a broad (still single) peak in (b), and double peaks in (c). We also calculated $\Psi(\rho)$ in equilibrium at the same temperatures, which exhibits double flattened peaks for $T = 0.5$ and sharper double peaks for $T = 0.48$, so the double peak behavior emerges more conspicuously in equilibrium. Furthermore, as a complicating factor in heat flow, Fig.5 indicates that the average density profile is considerably dependent on z in (b) and (c).
(ii) The momentum distribution $J_p(\rho)$ is positive for $\rho \gtrsim 0.37$ and negative for for $\rho \lesssim 0.37$. This is consistent with the anti-symmetric behavior, $J_p(\rho) \sim Q(\rho - 0.37)\Psi(\rho)$, close to the criticality in Eq.(C.5) of Appendix C. Evidently, the liquid-like clusters move toward the higher temperature boundary, while the particles in the gas-like regions move toward the lower temperature boundary. However, notice that the high-density maximum is considerably sharper than the low-density minimum, which should arise from the gas-liquid asymmetry of the fluctuations [22]. In particular, for the case (b), the momentum density of the liquid-like regions is of order 10^{-3} and the velocity is of order 3×10^{-3} (in units of $\sigma/\tau_0 = (\epsilon/m)^{1/2}$). In this case we have $\xi \sim 18$ and $D_T \sim 0.1$ so that the distance of the cluster motion within the life time $\xi^2/D_T \sim 3 \times 10^3$ is estimated to be of order 10.
(iii) The heat flux distribution function $J_Q(\rho)$ still exhibits considerable irregular behavior, but its negativity at any ρ is clear. Let us smooth out the curves; then, $J_Q(\rho)$ has a single minimum in (a) and double minima in (b) and (c). Thus, as $T \to T_{\rm c}$, heat is largely transported by the counterflow of the liquid-like clusters and the gas-like regions. Particularly in (c), the contribution from $\rho \cong 0.37$ becomes very small and the curve can be fairly fitted to the symmetric relation $J_Q(\rho) \sim -Q(\rho - 0.37)^2\Psi(\rho)$ in accord with Eq.(C.6). The gas-liquid asymmetry is more suppressed for $J_Q(\rho)$ than for $J_p(\rho)$.

IV. CONCLUDING REMARKS

MD simulations have been performed on LJ near-critical fluids in two dimensions. In equilibrium the critical properties obtained are presented in Figs.1-3. The main results under heat flow are summarized as follows.
(i) We have calculated the average density and temperature profiles in a steady state in Fig.4, where they are fairly fitted to linear lines and satisfy Eq.16. The density deviation is much enhanced than that of the temperature and the average pressure remains homogeneous.
(ii) We have obtained critical enhancement of the thermal conductivity for various T close to $T_{\rm c}$ in Figs.7 and 8 in good agreement with the mode-coupling prediction in Eq.19 derived in Appendix B.
(iii) We have calculated the one-body density distribution $\Psi(\rho)$, the momentum distribution $J_p(\rho)$, and the heat flux distribution $J_Q(\rho)$ defined by Eqs.21, 24, and 25. Fig.9 demonstrates the cluster convection mechanism, which is briefly summarized in the introduction and supported in Appendix C in the linear regime.
(iv) The cluster convection is a natural consequence of the irreversibility in heat conduction, while the density increase near the cooler boundary in Fig.6 arises from the simple thermodynamics under homogeneous pressure in Eq.16. These two effects are not contradictory with each other in view of the fact that the distance of cluster convection is very short.

The following problems could be mentioned as future subjects of nonequilibrium MD simulations.

(i) When the boundary wall is heated with a fixed cell volume, sound waves emitted from the boundary can cause rapid adiabatic heating throughout the cell (the piston effect) [27, 28]. We should examine how this phenomenon starts in the early stage on the acoustic time scale [2].
(ii) Heat conduction in two-phase near-critical fluids below T_c has been little examined in the literature [2]. For example, we should examine how a gas-liquid interface reacts to applied heat flow, where latent heat transport can be crucial in the presence of convection. Interestingly, gas bubbles in liquid migrate toward the warmer boundary in heat flow owing to the Marangoni effect [29].@

Acknowledgments

This work is supported by Grants in Aid for Scientific Research and for the 21st Century COE project (Center for Diversity and Universality in Physics) from the Ministry of Education, Culture, Sports, Science and Technology of Japan. Calculations have been performed at the Human Genome Center, Institute of Medical Science, University of Tokyo and the Supercomputer Center, Institute for Solid State Physics, University of Tokyo.

Appendix A: Microscopic Expressions

We introduce the momentum density,

$$\boldsymbol{J}(\boldsymbol{r},t)=\sum_i m\boldsymbol{v}_i(t)\delta(\boldsymbol{r}-\boldsymbol{r}_i(t)) \tag{A.1}$$

and the energy current density $\boldsymbol{J}^{\rm e}(\boldsymbol{r},t)$. The microscopic expression for the latter quantity is rather complicated [2]. Let us consider its space integral $\boldsymbol{J}^{\rm e}_0(t)=\int_{V_1} d\boldsymbol{r}\boldsymbol{J}^{\rm e}(\boldsymbol{r},t)$ in a subsystem with volume V_1 containing many particles. It may be approximated as

$$\begin{aligned}\boldsymbol{J}^{\rm e}_0(t) &= \frac{1}{2}{\sum_i}'\Big[mv_i^2+\sum_{j\neq i}\phi(r_{ij})\Big]\boldsymbol{v}_i \\ &- \frac{1}{2}{\sum_i}'\sum_{j\neq i}\phi'(r_{ij})\frac{1}{r_{ij}}(\boldsymbol{v}_i\cdot\boldsymbol{r}_{ij})\boldsymbol{r}_{ij},\end{aligned} \tag{A.2}$$

where $\boldsymbol{r}_i=\boldsymbol{r}_i(t)$ and $\boldsymbol{v}_i=\boldsymbol{v}_i(t)$ are the position and velocity of the i-th particle (the time t being suppressed in (A.2)), $\boldsymbol{r}_{ij}=\boldsymbol{r}_i-\boldsymbol{r}_j$, $\phi'(r)=d\phi(r)/dr$, and the summation ${\sum_i}'$ is over the particles contained in the subsystem under consideration. Here the pair interactions between the particles inside and outside the subsystem are not precisely accounted for.

The microscopic heat flux density is defined by [2]

$$\boldsymbol{J}^Q(\boldsymbol{r},t)=\boldsymbol{J}^{\rm e}(\boldsymbol{r},t)-[(e+p)/n]\boldsymbol{J}(\boldsymbol{r},t), \tag{A.3}$$

where e, p, and n are the average energy, pressure, and density, respectively. This current satisfies the orthogonal property $\int d\boldsymbol{r}\langle \boldsymbol{J}^Q(\boldsymbol{r},t)\cdot\boldsymbol{J}(\boldsymbol{r}',t)\rangle=0$ in equilibrium. The Green-Kubo formula for the thermal conductivity reads

$$\lambda=\frac{1}{k_{\rm B}T^2}\int_0^\infty dt\int d\boldsymbol{r}\langle J_z^Q(\boldsymbol{r},t)J_z^Q(\boldsymbol{0},0)\rangle. \tag{A.4}$$

The $J_0^{Qz}(t)$ in Eq.18 is the z component of the total heat flux in the interior,

$$\boldsymbol{J}_0^Q(t)=\int_{\rm interior} d\boldsymbol{r}\boldsymbol{J}^Q(\boldsymbol{r},t). \tag{A.5}$$

In Eqs.24 and 25 the space integrals are within small subsystems.

Appendix B: Mode-Coupling Theory

In the critical dynamics of simple fluids the gross variables include the long wavelength parts (with wave numbers in the region $q\ll\sigma^{-1}$) of the energy density $\hat{e}$, the particle density $\hat{n}$, and the momentum density $\boldsymbol{J}$. The heat flux density $\boldsymbol{J}^Q(\boldsymbol{r},t)$ in (A.3) has been approximated as a sum of a product of the gross variables and a random part in the form [2, 3, 4, 5],

$$\boldsymbol{J}^Q(\boldsymbol{r},t)=\frac{T}{m}\delta\hat{s}(\boldsymbol{r},t)\boldsymbol{J}(\boldsymbol{r},t)+\boldsymbol{J}^Q_{\rm R}(\boldsymbol{r},t). \tag{B.1}$$

The $\delta\hat{s}$ is the fluctuating entropy deviation (per particle) defined by

$$\delta\hat{s}(\boldsymbol{r},t)=\frac{1}{nT}\left[\delta\hat{e}(\boldsymbol{r},t)-\frac{e+p}{n}\delta\hat{n}(\boldsymbol{r},t)\right], \tag{B.2}$$

in terms of the deviations of the energy density $\hat{e}$ and the number density $\hat{n}$ The $\hat{e}$ can be defined microscopically using the particle positions and velocities [2, 24]. The first term on the right hand side of (B.1) evolves slowly in time and gives rise to the singular part of the thermal conductivity $\Delta\lambda$ when substituted into (A.4). In 2D the mode-coupling calculation yields the following integral over the wave vector $\boldsymbol{q}$,

$$\Delta\lambda=\frac{k_{\rm B}T}{2\eta}\int\frac{d\boldsymbol{q}}{(2\pi)^2}\frac{1}{q^2}C_p(q), \tag{B.3}$$

where η is the shear viscosity [25] and $C_p(q)=k_{\rm B}^{-1}n^2\langle|\hat{s}_{\boldsymbol{q}}|^2\rangle$ is the variance of the entropy fluctuation with $\hat{s}_{\boldsymbol{q}}$ being the Fourier component. See Appendix C for another derivation of $\Delta\lambda$ from the linear response. As far as the most singular part is concerned, we may set [2]

$$\delta\hat{s}\cong -n^{-2}(\partial p/\partial T)_{\rm cx}\delta\hat{n}. \tag{B.4}$$

This yields

$$C_p(q)\cong(\partial p/\partial T)^2_{\rm cx}S(q)/k_{\rm B}n, \tag{B.5}$$

in terms of the structure factor $S(q)$ in Eq.5 [2]. The long wavelength limit $C_p=\lim_{q\to0}C_p(q)$ is the usual isobaric specific heat per unit volume behaving as in Eq.10. Note that the integral (B.3) is logarithmically divergent

at small q, so we obtain the expression Eq.19. On the other hand, the second term on the right hand side of (B.1) relaxes rapidly and gives rise to the background thermal conductivity $\lambda_{\rm B}$.

Appendix C: Linear Response to Temperature Gradient near the Gas-Liquid Critical Point

Here we consider the linear response theory with respect to a temperature gradient $\boldsymbol{a} \equiv \nabla T$ (along the z axis) in a steady heat-conducting state in the absence of macroscopic velocity field [26]. To pick up the singular contribution near the gas-liquid critical point we may approximate the heat flux by $(T/m)\delta\hat{s}(\boldsymbol{r},t)\boldsymbol{J}(\boldsymbol{r},t)$ from (B.1). Then the linear response of any dynamic variable $\mathcal{B}(\boldsymbol{r},t)$ to $\boldsymbol{a}$ can be written as [2]

$$\delta\langle\mathcal{B}\rangle = \frac{-\boldsymbol{a}}{mk_{\rm B}T}\cdot\int_0^\infty dt\int d\boldsymbol{r}'\langle\mathcal{B}(\boldsymbol{r},t)\delta s(\boldsymbol{r}',0)\boldsymbol{J}(\boldsymbol{r}',0)\rangle$$
$$= \frac{\boldsymbol{a}}{mk_{\rm B}T}\cdot\int_0^\infty dt\int d\boldsymbol{r}'\langle\tilde{\mathcal{B}}(\boldsymbol{r},0)\delta s(\boldsymbol{r}',t)\boldsymbol{J}(\boldsymbol{r}',t)\rangle. \quad \text{(C.1)}$$

From the first to second line use has been made of the time-reversal relation $\langle\mathcal{A}(t)\mathcal{B}(0)\rangle = \langle\tilde{\mathcal{B}}(t)\tilde{\mathcal{A}}(0)\rangle$ where $\tilde{\mathcal{A}}$ and $\tilde{\mathcal{B}}$ are the time-reversed variables. For example, $\tilde{\boldsymbol{J}} = -\boldsymbol{J}$. Furthermore, on the second line, we may replace $\delta s(\boldsymbol{r}',t)$ by $\delta s(\boldsymbol{r}',0)$ because the relaxation time of $\boldsymbol{J}(\boldsymbol{r}',t)$ due to the shear viscosity η is much faster than that of $\delta s(\boldsymbol{r}',t)$. Then the time integral may be performed to give

$$\delta\langle\mathcal{B}\rangle = -\sum_{ij}\frac{na_i}{k_{\rm B}T}\int d\boldsymbol{r}'\int d\boldsymbol{r}''\mathcal{T}_{ij}(\boldsymbol{r}'-\boldsymbol{r}'')$$
$$\times\langle\mathcal{B}(\boldsymbol{r})\delta s(\boldsymbol{r}')J_j(\boldsymbol{r}'')\rangle, \quad \text{(C.2)}$$

where the equal-time correlation is involved and the time dependence is hence suppressed. The $\mathcal{T}_{ij}(\boldsymbol{r})$ is the Oseen tensor whose Fourier transformation is $\mathcal{T}_{ij}(\boldsymbol{q}) = (\delta_{ij} - q_iq_j/q^2)/\eta q^2$. In 3D it follows the well-known expression $\mathcal{T}_{ij}(\boldsymbol{r}) = (\delta_{ij} + x_ix_j/r^2)/8\pi\eta r$.

In (C.2), if we set $\mathcal{B} = (T/m)\delta\hat{s}J_z$ and use the equilibrium relation $\langle J_i(\boldsymbol{r})J_j(\boldsymbol{r}')\rangle = k_{\rm B}T\rho\delta_{ij}\delta(\boldsymbol{r}-\boldsymbol{r}')$, we reproduce the mode-coupling expression for the singular part of the thermal conductivity (given by (B.3) in 2D) in the form $\delta\langle\mathcal{B}\rangle = -\Delta\lambda dT/dz$. Next let us set $\mathcal{B} = J_z\delta(\rho-\hat{n})$ and $J_z^Q\delta(\rho-\hat{n})$ where the dynamic variables J_z, J_z^Q, and $\hat{n}$ are the coarse-grained quantities averaged in appropriate cells. Then we obtain $J_p(\rho)$ and $J_Q(\rho)$ in Eqs.24 and 25 expressed as

$$J_p(\rho) = m\left(\frac{\partial p}{\partial T}\right)_{\rm cx}\frac{dT}{dz}\int d\boldsymbol{r}'\mathcal{T}_{zz}(\boldsymbol{r}-\boldsymbol{r}')$$
$$\times\langle\delta(\rho-\hat{n}(\boldsymbol{r}))\delta n(\boldsymbol{r}')\rangle, \quad \text{(C.3)}$$

$$J_Q(\rho) = -\frac{T}{n^2}\left(\frac{\partial p}{\partial T}\right)_{\rm cx}^2\frac{dT}{dz}\int d\boldsymbol{r}'\mathcal{T}_{zz}(\boldsymbol{r}-\boldsymbol{r}')$$
$$\times\langle\delta(\rho-\hat{n}(\boldsymbol{r}))\delta n(\boldsymbol{r})\delta n(\boldsymbol{r}')\rangle. \quad \text{(C.4)}$$

We notice that these quantities depend on the cell volume $V_{\rm cell}$. If the cell length $\ell_{\rm cell} = V_{\rm cell}^{1/d}$ is shorter than the correlation length ξ, we estimate $J_p(\rho)$ as

$$J_p(\rho) \sim \frac{m}{\eta}\ell_{\rm cell}^2(\rho-n_{\rm in})\Psi(\rho)\left(\frac{\partial p}{\partial T}\right)_{\rm cx}\frac{\partial T}{\partial z}, \quad \text{(C.5)}$$

where $n_{\rm in}$ is the average density. If $\ell_{\rm cell}$ is longer than ξ, we divide the cell into subsystems with length ξ and find that $J_p(\rho)$ is given by (C.5) with $\ell_{\rm cell}^2$ being replaced by ξ^2. Next notice that the integral $\int d\rho J_Q(\rho)$ is equal to $-(\Delta\lambda)dT/dz$ from (C.4) which is in accord with Eq.28 for $\Delta\lambda \cong \lambda$. Accounting for this sum rule we thus expect

$$J_Q(\rho) \cong -A_Q(\rho-n_{\rm in})^2\Psi(\rho)\frac{\partial T}{\partial z}, \quad \text{(C.6)}$$

for $\ell_{\rm cell} \ll \xi$. The coefficient A_Q is determined from the normalization condition Eq.28. The estimations (C.5) and (C.6) are consistent with the data in Fig.9.

In addition, Eq.1 in the introduction follows if we assume $v_\xi \sim J_p(\rho)/mn\Psi(\rho)$ in (C.5) by setting $\ell_{\rm cell} \sim \xi$ and $\rho - n_{\rm in} \sim \xi^{-\beta/\nu}$ with the aid of the exponent relation $2\beta = (d-2+\hat{\eta})\nu$ [2]. Note that $J_p(\rho)/\Psi(\rho)$ represents the average momentum density at density ρ.

Appendix D: Diffusion in Two Dimensions

In two dimensions the flux-time correlation functions for the transport coefficients have a long time tail relaxing as $1/t$, giving rise to a logarithmic singularity (if integrated over time) [25]. The simplest example is the diffusion constant D of a tagged particle. It is the time integral of the velocity time-correlation function,

$$G(t) = \frac{1}{2N}\sum_{i=1}^N\langle\boldsymbol{v}_i(t_0+t)\cdot\boldsymbol{v}_i(t_0)\rangle. \quad \text{(D.1)}$$

The long time tail of $G(t)$ is theoretically given by $(k_{\rm B}T/8\pi\eta)/t$ if the kinetic viscosity η/mn is much larger than D. By taking the average over t_0 in a time interval of 5×10^4, we obtained $\int_0^t dt'G(t') \cong 0.17 + 0.059\log t$ for $t \gtrsim 1$, leading to $k_{\rm B}T/8\pi\eta = 0.059$. Note that the kinetic viscosity is close 1 and is considerably larger than the diffusion constant in our system.

[1] J.V. Sengers and J.M.H. Levelt Sengers, in *Progress in Liquid Physics,* edited by C.A. Croxton (Wiley, Chichester, England, 1978).

[2] A. Onuki, *Phase Transition Dynamics* (Cambridge University Press, Cambridge, 2002).

[3] L.P. Kadanoff and J. Swift, Phys. Rev. **166**, 89 (1968).

[4] K. Kawasaki, in *Phase Transition and Critical Phenomena*. edited by C. Domb and M.S. Green (Academic, New York, 1976), Vol.5A; Ann. Phys. (N.Y.) **61**, 1 (1970).

[5] E.D. Siggia, B.I. Halperin, and P.C. Hohenberg, Phys. Rev. B **13**, 2110 (1976).

[6] J.P. Hansen and I.R. McDonald, *Theory of Simple Liquids*, (Academic Press, London, 1986).

[7] M.P. Allen and D.J. Tildesley, *Computer Simulation of Liquids* (Clarendon Press, Oxford, 1987).

[8] R. Vogelsang, C. Hoheisel, G. V. Paolini, and G. Ciccotti, Phys. Rev. A **36**, 3964 (1987); R. Vogelsang, C. Hoheisel, and G. Ciccotti, J. Chem. Phys. **86**, 6371 (1987).

[9] P. J. Gardner, D. M. Heyes, and S. R. Preston, Mol. Phys. **73**, 141 (1991).

[10] G. V. Paolini, G. Ciccotti, and C. Massobrio, Phys. Rev. A **34**, 1355 (1986).

[11] D. J. Evans and S. Murad, Mol. Phys. **68**, 1219 (1989); B. Y. Wang, P. T. Cummings, and D. J. Evans, Mol. Phys. **75**, 1345 (1992).

[12] B. Hafskjold, T. Ikeshoji, and S. K. Ratkje, Mol. Phys. **80**, 1389 (1993); T. Ikeshoji and B. Hafskjold. ibid. **81**, 251 (1994).

[13] T. Ohara, J. Chem. Phys. **111**, 9667 (1999).

[14] T. Ohara, J. Chem. Phys. **111**, 6492 (1999).

[15] J.A. Barker, D. Henderson, and F.F. Abraham, Physica **106A**, 226 (1981).

[16] R.R. Singh, K.S. Pitzer, J.J. de Pablo, and J.M. Prausnitz, J. Chem. Phys. **92**, 5463 (1990).

[17] B. Smit and D. Frenkel, J. Chem. Phys. **94**, 5663 (1990).

[18] S. Jiang, and K.E. Gubbins, Molec. Phys. **86**, 599 (1995).

[19] M. Rovere, J. Phys.; Condens. Matt. **5**, B193 (1993); M. Rovere, P.Nielaba, and K. Binder, Z. Phys. **90**, 215 (1993).

[20] H. Luo, G. Ciccotti, M. Mareschal, M. Meyer, and B. Zappoli, Phys. Rev. E **51**, 2013 (1995).

[21] S. Nóse, Molec. Phys. **52**, 255 (1983).

[22] On the critical isochore $(\partial p/\partial T)_n/(\partial p/\partial T)_{\rm cx} - 1$ is of order $C_v/C_p \sim (T/T_{\rm c} - 1)^{\gamma-\alpha}$ [2], where $\gamma = 7/4$ and $\alpha = 0$ in two dimensions.

[23] In Ising spin systems we may equally define clusters with up-spins and those of down-spins. In our simulations, however, only the denser clusters ($n > n_{\rm c}$) are well defined as in Fig.5. The symmetry between the higher-density and lower-density critical fluctuations should be attained much closer to the criticality.

[24] N.B. Wilding, J. Phys. Condens. Matt. **9**, 585 (1997).

[25] B. J. Alder and T. E. Wainwright Phys. Rev. A **1**, 18 (1970); J. R. Dorfman and E. G. D. Cohen, Phys. Rev. Lett. **25**, 1257 (1970); T. E. Wainwright, B. J. Alder, and D. M. Gass, Phys. Rev. A **4**, 233 (1971). The shear viscosity also has a small logarithmic singularity $\eta = \eta_0 + A_\eta \log(L/\sigma)$ with $A_\eta/\eta_0 \sim mnk_{\rm B}T/8\pi\eta_0^2$ being small.

[26] I. Procaccia, D. Ronis, M.A. Collins, J. Ross, and I. Oppenheim, Phys. Rev. A **19**, 1290 (1979).

[27] A. Onuki, H. Hao and R. A. Ferrell, Phys. Rev. A **41**, 2256 (1990).

[28] Y. Garrabos, M. Bonetti, D. Beysens, F. Perrot, T. Fröhlich, P. Carlès, and B. Zappoli, Phys. Rev. E **57**, 5665 (1998).

[29] D. Beysens, Y. Garrabos, V. S. Nikolayev, C. Lecoutre-Chabot, J.-P. Delville, and J. Hegseth, Europhys. Lett., **59**, 245 (2002).

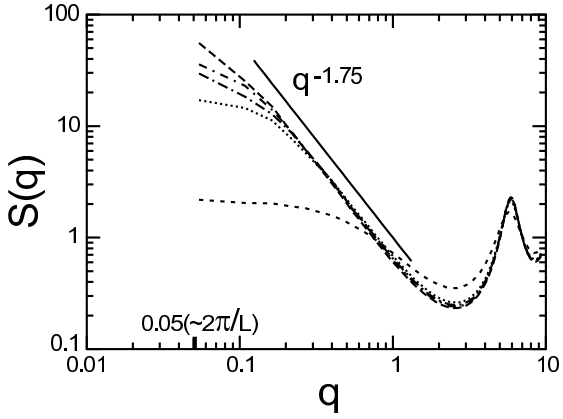

FIG. 1: The structure factor $S(q)$ at@ $n = 0.37$ for $T = 0.65$ (short-dashed line at bottom), 0.51, 0.5, 0.495, and 0.49 (dashed line on top). A line with a slope of $-7/4$ is included as a guide.

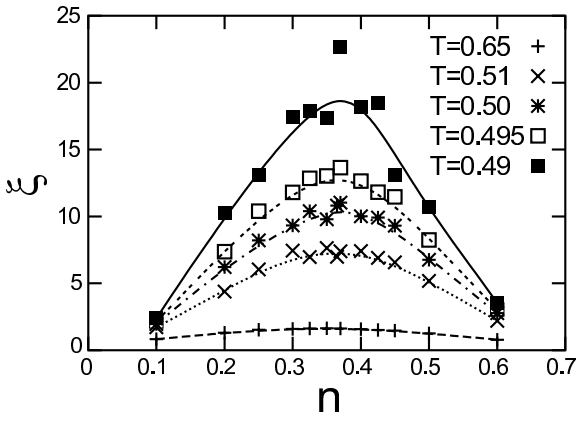

FIG. 2: The correlation length ξ vs the density at various temperatures obtained from the structure factor.

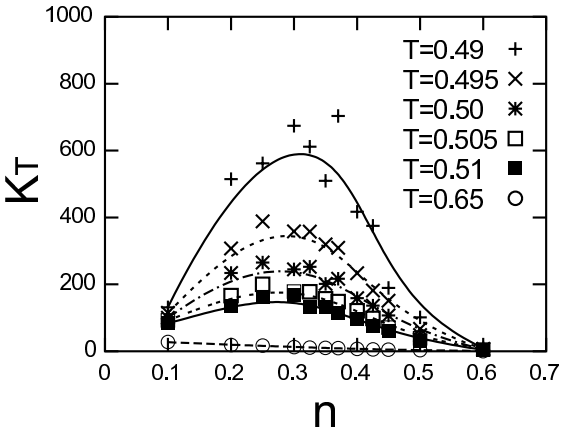

FIG. 3: The isothermal compressibility K_T vs the density at various temperatures obtained from the structure factor.

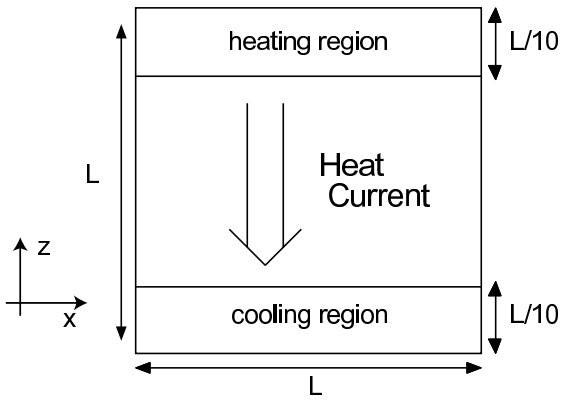

FIG. 4: Simulation cell under heat flow composed of cooling, heating, and interior regions[13].

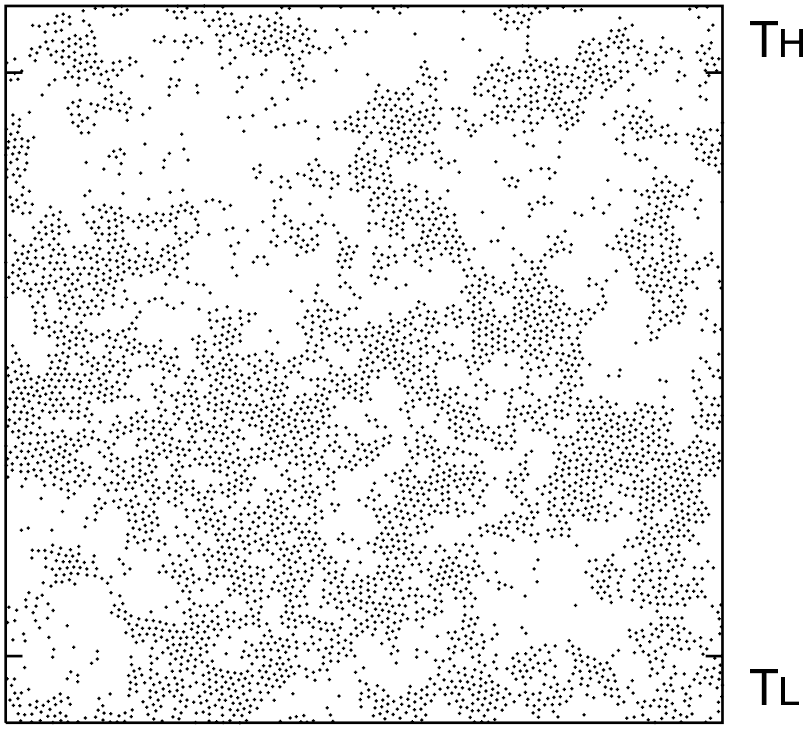

FIG. 5: Snapshot of the particle configuration at $n = 0.37$ in a steady state with $T_{\rm L} = 0.50$ and $T_{\rm H} = 0.505$. The horizontal bars at the vertical box lines mark the boundary between the interior region and cooling or heating region.

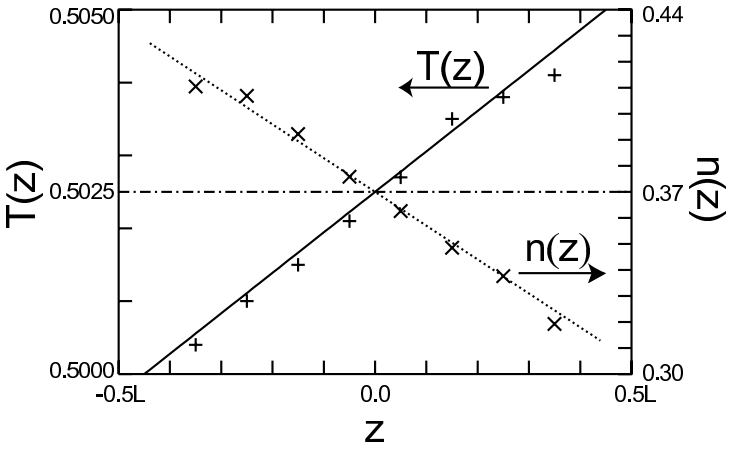

FIG. 6: Steady-state temperature and density profiles in the z-direction obtained by the time average. The solid line has a slope of $\Delta T/(9L/10)$ with $\Delta T = 0.005$, while the dotted line has a slope of $-n\alpha_p \Delta T/(9L/10)$ in Eq.16.

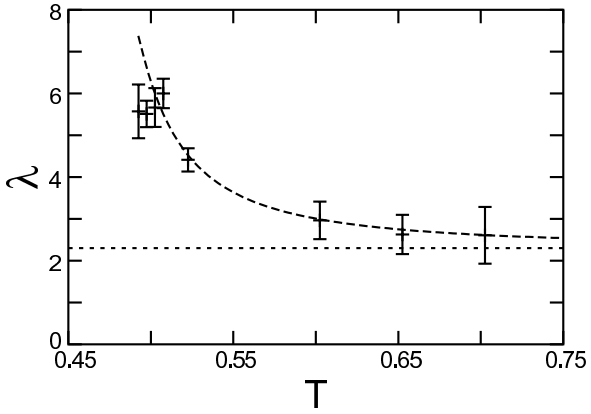

FIG. 7: The thermal conductivity λ calculated from Eqs.16 and 17 at $n = 0.37$ for $T = 0.7$, 0.65, 0.6, 0.52, 0.51, 0.5, 0.495, and 0.49. The bold dashed line is a view guide. The width of each error bar is twice of the variance of 10 data values corresponding to 10 independent runs.

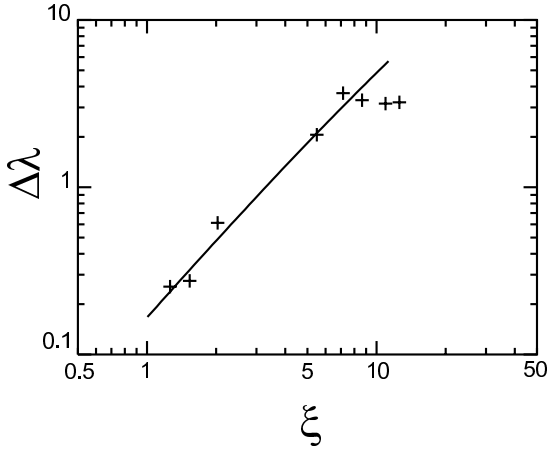

FIG. 8: The singular part of the thermal conductivity $\Delta\lambda$ as a function of ξ on logarithmic scales. The solid line is the second term in Eq.19 with $A_\lambda = 0.035$.

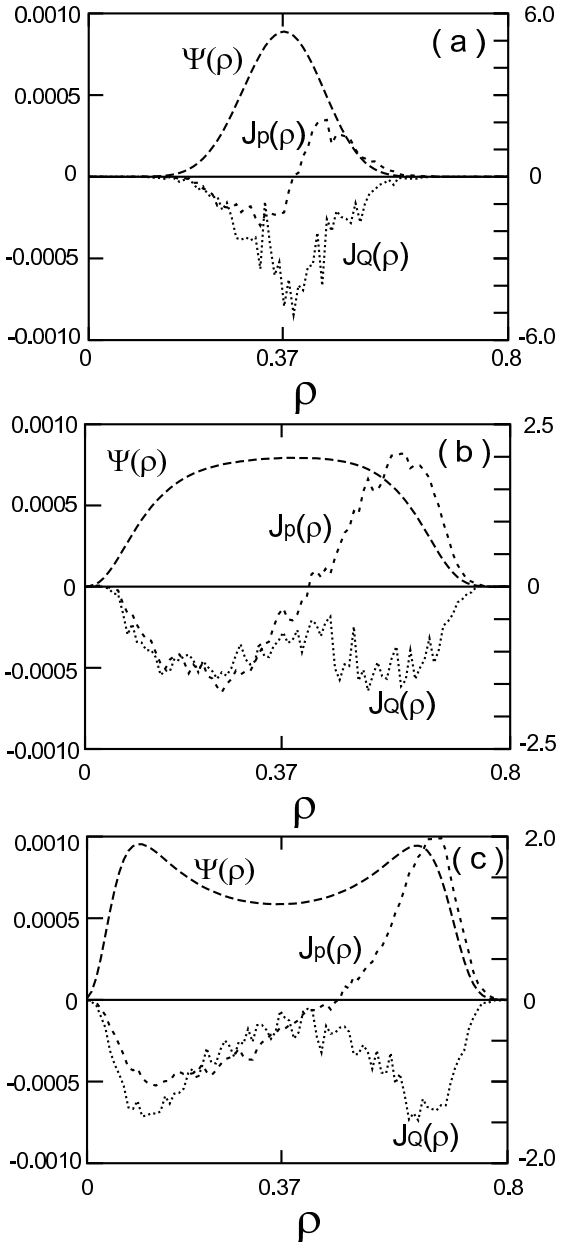

FIG. 9: (a) Density distribution function $\Psi(\rho)$ (right scale), momentum distribution $J_p(\rho)$, and heat-flux distribution $J_Q(\rho)$ (left scale) obtained at $n = 0.37$ for $T_{\rm L} = 0.65$ in (a), $T_{\rm L} = 0.50$ in (b), and $T_{\rm L} = 0.48$ in (c).